


## Probing nanoscale variations in strain and band structure of MoS<sub>2</sub> on Au nanopillars using tip-enhanced Raman spectroscopy

Zhongjian Zhang, Alex C. De Palma, Christopher J. Brennan, Gabriel Cossio, Rudresh Ghosh, Sanjay K. Banerjee, and Edward T. Yu

*Microelectronics Research Center, University of Texas, Austin, Texas, 78758, USA*

 (Received 25 October 2017; revised manuscript received 18 January 2018; published 12 February 2018)

We report tip-enhanced Raman spectroscopy and tip-enhanced photoluminescence studies of monolayer and bilayer MoS<sub>2</sub> in which we characterize photoluminescence and first- and second-order Raman spectra in monolayer, bilayer, and inhomogeneously strained MoS<sub>2</sub>. From the transition of unstrained MoS<sub>2</sub> from monolayer to bilayer, we determine a spatial resolution of approximately 100 nm through the peak positions of the first-order Raman modes. The strain dependence of the second-order Raman modes reveals changes in the electronic band structure in strained MoS<sub>2</sub> that are directly observed through changes in the Raman peak positions and peak area ratios, which are corroborated through density functional theory calculations.

DOI: [10.1103/PhysRevB.97.085305](https://doi.org/10.1103/PhysRevB.97.085305)

### I. INTRODUCTION

Phonons in atomically thin transition-metal dichalcogenides (TMDCs) are directly affected by a wide range of material characteristics including number of layers, strain, electronic band structure, and defects. Raman spectroscopy is a powerful tool to directly detect these and various other material properties through the interaction of incident light and phonons [1,2]. Resonance Raman (RR) scattering, in which the excitation wavelength is tuned near the energy of electronic transitions, probes additional changes in the electronic and physical structure not normally detected in conventional Raman scattering [1]. In addition, photoluminescence (PL) peaks that can be present in resonant Raman spectra can provide further information about structural features, such as grain boundaries [3,4] and defects [5].

In conventional Raman spectroscopy measurements, the spatial resolution that can be achieved is limited by diffraction and by the weakness of Raman scattering processes, which limits signal intensity for small excitation volumes [1,2]. Tip-enhanced Raman spectroscopy (TERS) enables dramatic improvement in spatial resolution when compared to conventional Raman spectroscopy by employing a metallic nanostructure at the apex of an atomic force microscope probe tip to induce plasmonic localization and amplification of incident light in the immediate vicinity of the probe tip [6–9]. The plasmonic enhancement induced by the metallic probe can also allow near-field PL measurements to be performed with significantly enhanced spatial resolution [10]. In addition, the combination of atomic force microscopy (AFM) and light scattering spectroscopy techniques in a single measurement apparatus allows information concerning structural, electrical, or other properties that can be probed at the nanoscale using AFM and related techniques to be correlated with that gleaned from TERS and nano-PL measurements that can be performed with similar spatial resolution.

The high spatial resolution and precise positional control attained in TERS are especially useful to characterize mate-

rials such as atomically thin two-dimensional (2D) TMDCs, because of the nanoscale variations in strain, layer thickness, and electronic structure that can be present. Two-dimensional TMDCs can also sustain large elastic deformations before rupture of the material [11,12], which allows realization of localized regions of high strain. Among 2D TMDCs, MoS<sub>2</sub> shows a large intrinsic band gap that makes it suitable for various electronic and optoelectronic devices [13–15]. The band structure of MoS<sub>2</sub> is also highly sensitive to strain [16], which highlights the importance of localized detection of strain when designing devices. Strain engineering has been employed, for example, to demonstrate efficient quantum emitters in other TMDCs, such as WSe<sub>2</sub> and WS<sub>2</sub>, with enhanced PL intensity [17,18]. Characterization of nanoscale strain distribution is also relevant to investigation of electromechanical effects in atomically thin TMDCs [19–21]. Conventional Raman measurements on MoS<sub>2</sub> have previously been used to measure changes in strain and band structure through Raman and PL measurements, but generally with low spatial or spectral precision [16,22]. Specifically in MoS<sub>2</sub>, RR scattering reveals a complex variety of second-order Raman features that can yield additional information about the physical properties and electronic band structure [23,24].

We have performed localized characterization of thickness, strain, and band structure of monolayer and bilayer MoS<sub>2</sub> using TERS, through both the first-order and second-order Raman modes, as well as tip-enhanced photoluminescence (TEPL). By combining Raman spectroscopy with a scanning probe technique, we can dramatically increase positional precision while simultaneously achieving superior spatial resolution. Using AFM, we identify a region of MoS<sub>2</sub> that transitions from monolayer to bilayer and perform TERS measurements that accurately distinguish sample thickness with spatial resolution well below the diffraction limit. We also observe a previously unreported negative shift in the second-order acoustic phonon Raman band at the interface between monolayer and bilayer regions. After applying strain to bilayer MoS<sub>2</sub> by draping the sample over patterned Au nanopillars, we detect changes

in strain across a half-micron region with a spatial resolution well below the diffraction limit using both TERS and TEPL through the negative shift in the first-order Raman modes and the change in intensity of the PL spectra that occurs in isolated regions of higher tensile strain. We also show in detail the strain dependences of the second-order Raman modes in MoS<sub>2</sub> that further reveal changes in the band structure of MoS<sub>2</sub> induced by applied strain. Finally, we perform density functional theory (DFT) simulations that show that the strain-dependent changes in the second-order Raman spectra directly correlate with strain-dependent changes in the band structure and phonon dispersion.

## II. EXPERIMENTAL DETAILS

The MoS<sub>2</sub> characterized in these experiments was grown on SiO<sub>2</sub> substrates by a standard vapor transfer growth process with MoO<sub>3</sub> (15 mg) and sulfur (1 g) powder as the starting materials resulting in MoS<sub>2</sub> layers of varying thicknesses. Further information on growth details can be found in Ref. [25]. MoS<sub>2</sub> was transferred from the growth substrate to either a flat Au substrate or a patterned Au nanopyramid substrate using a Polydimethylsiloxane (PDMS) stamp and water transfer process. The as-grown MoS<sub>2</sub> is under approximately 0.21% residual tensile strain [26], which is relaxed under the transfer process. The PDMS stamp is applied to a region of the growth substrate with atomically thin MoS<sub>2</sub>. To separate the MoS<sub>2</sub> from the growth substrate, the substrate, MoS<sub>2</sub>, and stamped PDMS are placed in a water bath. The PDMS stamp with the MoS<sub>2</sub> is then pressed onto either the flat or patterned Au substrate and heated with a hot plate to 50°C. Slowly peeling away the PDMS transfers the MoS<sub>2</sub> to the substrate. (A schematic drawing of the transfer process is shown in the Supplemental Material [27], Fig. S1.)

Au nanopyramids were fabricated via nanosphere lithography. First, a clean Petri dish was filled approximately three-quarters full with de-ionized (DI) water. A glass slide was then inserted into the Petri dish so that one end rested on the bottom surface of the dish and the other end was exposed to air resting on the rim of the Petri dish. A solution of equal parts 99.5% anhydrous ethanol and 1- $\mu$ m polystyrene nanospheres (3% coefficient of variance, 2.6% solids-latex from Polysciences Inc.) was made and micropipetted onto the glass slide in small increments. The solution is then allowed to thin out and roll down the glass slide and enter the bulk DI water. A strong surface tension gradient between the ethanol-nanosphere solution and the DI water causes the nanospheres to self-assemble into  $\sim 1 - \text{cm}^2$  monolayers on the air-water interface. A silicon substrate was then used to “scoop up” the monolayers of nanospheres onto the substrate surface. The wet monolayer was left to dry under a heat lamp. The hexagonal array of nanospheres was then used as a mask for electron-beam evaporation of  $\sim 100$  nm of Al<sub>2</sub>O<sub>3</sub> to form the nanopyramid structure. The sample was then sonicated in toluene for 10 s to dissolve the nanospheres and reveal the Al<sub>2</sub>O<sub>3</sub> nanopyramids. Finally, a 5-nm/65-nm thick bilayer of Cr/Au was deposited using electron-beam deposition to cover the entire surface. This resulted in a relatively uniform array of Au nanopyramids on the surface. (Schematic and further

discussion on the nanopyramid fabrication process is found in Sec. 2 of the Supplemental Material [27].)

All Raman spectroscopy and photoluminescence measurements were performed with a Horiba LabRAM confocal Raman system with a backscattering geometry with *both 300 and 1800 grooves/mm gratings* using a vertically polarized HeNe laser at an excitation wavelength of 633 nm. MoS<sub>2</sub> regions characterized by TERS were first located by AFM topographic scanning in tapping mode with an AIST-NT Omegascope, which was also used to determine layer thickness and locate changes in topography. For TERS measurements, a mirror switch was used to send the same excitation laser to a set of external mirrors that illuminate the AFM tip in the Omegascope. A 100 $\times$  side objective illuminated our AFM tip at an angle of 30° relative to the surface of the sample with a spot size of  $\sim 1 \mu\text{m}$  and an incident laser power density of  $\sim 15 \text{ kW/cm}^2$ . Figure 1(a) shows a schematic diagram of the experimental setup with tip and sample geometries for TERS measurements of MoS<sub>2</sub> on a patterned Au nanopyramid sample. Because the sample stage moves instead of the tip, optical alignment is maintained throughout. Figure 1(b) shows a scanning electron microscopy (SEM) image of a typical tip, from which we estimate the tip radius of curvature from the image to be about 50 nm. TERS and TEPL measurements were taken with the tip in soft contact with the sample surface to maximize signal enhancement. Gold-coated AFM probe tips used in experiments were purchased commercially and first tested to demonstrate signal enhancement on a carbon nanotube reference sample.

## III. RESULTS AND DISCUSSION

Figures 1(c) and 1(d) show Raman spectra from monolayer and bilayer regions of MoS<sub>2</sub>, respectively. The red curves indicate spectra taken with the Au AFM probe in tapping mode with a 15-nm tapping amplitude. The black curves indicate spectra taken with the Au AFM probe in soft contact mode, which is the condition with which all TERS and TEPL data reported here were taken. Measurements taken in soft contact show a dramatic increase in Raman signal when compared to measurements taken in tapping mode. When the tip is placed into soft contact with the sample surface, the distance between the Au tip and the Au substrate decreases to a few nanometers, which allows a gap mode to form between the tip and substrate with strong enhancement of the *electromagnetic (EM)* field within that region that greatly increases the Raman signal as well as the background luminescence [28]. The significant signal enhancement indicates that by placing the probe tip in very close proximity to the sample, we can increase both signal localization and local excitation intensity.

Figure 2(a) shows a TERS spectrum for bilayer MoS<sub>2</sub> on a flat Au substrate that has been fit to seven Lorentzian peaks to estimate the spectral positions of the various Raman modes. The peaks have been numbered and assigned a corresponding vibrational mode, listed in Table I, that have been identified experimentally and theoretically in Ref. [24]. In our RR regime, the first-order in-plane  $E_{2g}^1$  mode centered at  $\sim 380 \text{ cm}^{-1}$ , labeled peak 1, displays some asymmetry but we found it is still best to analyze the spectral position by fitting with one Lorentzian peak. Peak 2, centered at  $\sim 405 \text{ cm}^{-1}$ ,

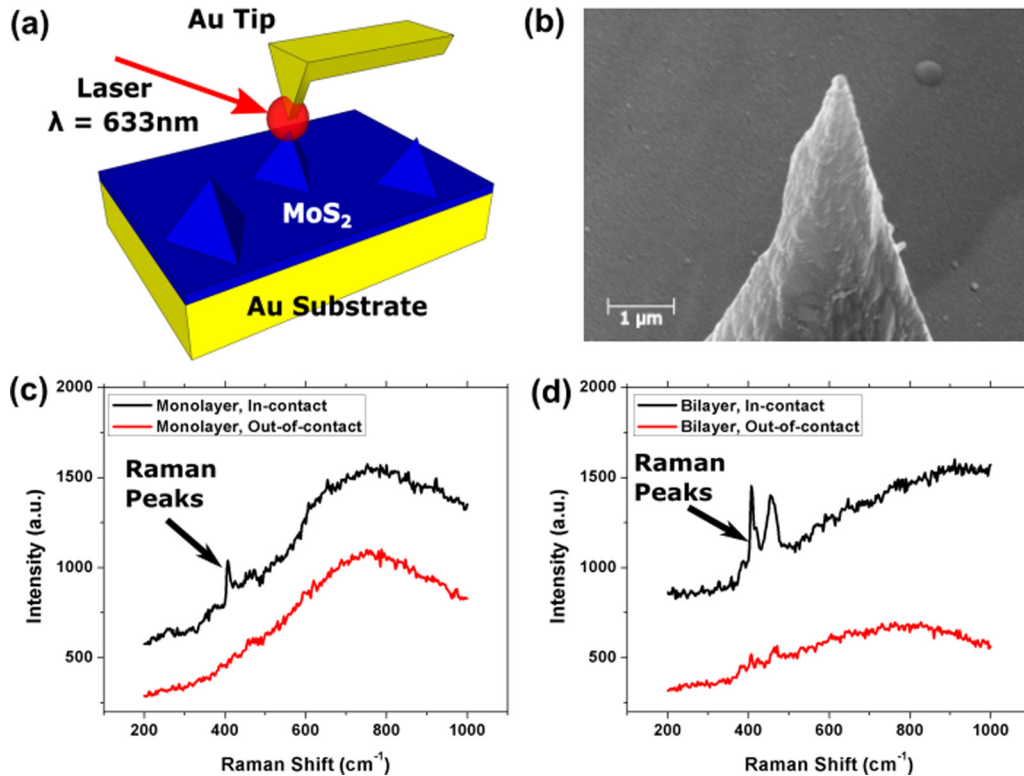


FIG. 1. (a) Schematic diagram of the experimental geometry for TERS measurements of MoS<sub>2</sub> draped over Au nanopyramid structures. (b) SEM image of a representative Au tip used for TERS and TEPL measurements. Raman spectra obtained with the Au AFM probe in tapping mode (red curve) and in soft contact with the sample surface (black curve) with a 300 grooves/mm grating from (c) monolayer MoS<sub>2</sub> and (d) bilayer MoS<sub>2</sub>.

represents the out-of-plane  $A_{1g}$  vibrational mode. The remaining peaks represent second-order Raman modes, which we emphasize we fit to single Lorentzians for convenience, since second-order modes generally involve convolutions of multiple interactions.

Most of the second-order Raman modes represent double resonance Raman (DRR) interactions that occur due to intervalley resonant scattering of the excited electrons by phonons when the excitation laser energy is near the  $B$  exciton energy

[24]. As shown in Fig. 2(b), an example DRR process starts when an incoming photon excites an electron-hole pair near the  $K$  valley of the Brillouin zone (BZ). The excited electron is then inelastically scattered to the  $K'$  valley by the emission of a phonon. After the first scattering process, the excited electron is inelastically scattered back to the  $K$  valley by the emission of a second phonon, where then the electron-hole pair recombines and emits a photon. Which phonons can mediate this scattering interaction is governed by energy and momentum conservation

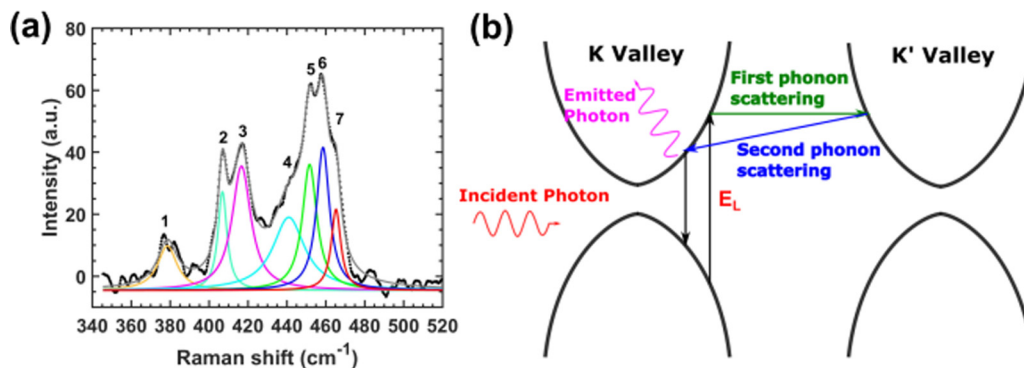


FIG. 2. (a) TERS spectrum from bilayer MoS<sub>2</sub> taken with an 1800 grooves/mm grating. The TERS spectrum has been fit to seven Lorentzian peaks with the numerical labels corresponding to vibrational modes listed in Table I. The sum of the fitted peaks is shown in gray and shows excellent agreement with the measured spectrum. (b) Schematic drawing of an example DRR process in which an incident photon of energy  $E_L$  first excites an electron-hole pair in the  $K$  valley; then the excited electron is scattered to the  $K'$  valley through the emission of the phonon, as shown with the green arrow. The excited electron is then scattered back to the  $K$  valley through the emission of a second phonon, as shown with the blue arrow. Finally, the electron-hole pair recombines and emits a photon.

TABLE I. Vibrational modes corresponding to fitted Lorentzian peaks shown in Fig. 2(a). Peak assignments, where indicated, are obtained from Ref. [24].

Peak number	Vibrational modes
1	$E_{2g}^1$
2	$A_{1g}$
3	LA( $\sim K$ ) + TA( $\sim K$ ) [24]
4	$A_{1g} + E_{2g}^2$ or possibly asymmetry from peak 5 [24]
5	Van Hove singularity in the phonon DOS [24]
6	2LA( $\sim K$ ) [24]
7	2LA( $\sim M$ ) [24]

constraints. In our work, the DRR process describes the scattering of excited electrons by longitudinal acoustic (LA) and transverse acoustic (TA) phonons associated with Raman modes represented by peaks 3, 6, and 7 [24].

From Ref. [24] and as listed in Table I, we associate peak 3, centered at  $\sim 420 \text{ cm}^{-1}$ , with intervalley scattering of excited electrons near the  $K$  point in the BZ by a combination of LA and TA phonons. Peak 4, centered at  $\sim 445 \text{ cm}^{-1}$ , represents either a combination of the  $A_{1g}$  and  $E_{2g}^2$  vibrational modes or an asymmetry related to peak 5. Peak 5, centered at  $\sim 455 \text{ cm}^{-1}$ , represents a Van Hove singularity in the phonon density of states (DOS) corresponding to a saddle point between the  $M$  and  $K$  points in the BZ. Finally, peak 6, centered at  $\sim 465 \text{ cm}^{-1}$ , and peak 7, centered at  $\sim 470 \text{ cm}^{-1}$ , represent intervalley scattering of excited electrons by two LA phonons near the  $K$  point and  $M$  point of the BZ, respectively. Each Raman mode yields unique information about the sample. We observe all the first- and second-order Raman modes in all TERS measurements in both monolayer and bilayer MoS<sub>2</sub>.

Figures 3(a) and 3(b) show contour plots of the conduction band edge energies from the band structure in monolayer and bilayer MoS<sub>2</sub>, respectively, calculated from DFT simulations. The conduction band minimum at the  $Q$  point in the BZ decreases in energy relative to the conduction band minimum at the  $K$  point in the BZ from monolayer to bilayer. Figure 3(c)

shows a cut of the band structure for the high-symmetry directions and points ( $\Gamma$ ,  $Q$ ,  $K$ ,  $M$ ) in the BZ for unstrained,  $-0.5\%$  applied hydrostatic strain, and  $+0.5\%$  applied hydrostatic strain bilayer MoS<sub>2</sub>. The strain behavior of the conduction band minima at the various high-symmetry points varies, most notably with a larger decrease in the conduction band minimum at the  $K$  point relative to the decrease at the  $Q$  point with higher applied strain. The strain dependence of the band structure agrees with previous theoretical work on bulk MoS<sub>2</sub>, which has a similar band structure to bilayer MoS<sub>2</sub> [29].

### A. Unstrained MoS<sub>2</sub>

Figure 4(a) shows an AFM image of MoS<sub>2</sub> that has been transferred onto a flat Au substrate. The region shown features both monolayer and bilayer regions where the solid white line indicates a line cut across a transition region from monolayer to bilayer. The topography along the line cut, shown in Fig. 4(b), indicates a clear change in thickness of the sample with a step height of approximately 0.6 nm, which is consistent with the layer thickness of MoS<sub>2</sub> of 0.65 nm found in previous AFM measurements [30]. An optical image of the larger sample area is shown in Fig. S2(a) in the Supplemental Material [27].

TEPL and TERS measurements were taken along the same line cut indicated in Fig. 4(a). The layer thickness of MoS<sub>2</sub> is directly detectable using PL and Raman spectroscopy, with PL measurements showing a general decrease in PL intensity [31,32] with increasing layer thickness. In particular, MoS<sub>2</sub> exhibits a transition from direct band gap for monolayer thickness to indirect band gap for bilayer thickness, which leads to clear differences in both the PL intensity [31,32] and a shift in the  $A$  excitonic peak to longer wavelengths [26] in the PL spectra between monolayer and bilayer MoS<sub>2</sub>. The top panel of Fig. 4(c) shows the position of the  $A$  excitonic PL peak and the peak PL intensity of TEPL measurements taken along the line cut indicated in Fig. 4(a). The  $A$  excitonic PL peak, which is associated with emission from both the uncharged excitons and charged excitons (trions) of the  $A$  excitonic transition [33], is fit to one Lorentzian to determine the peak position. The behavior of the PL peak position and the PL intensity clearly indicates

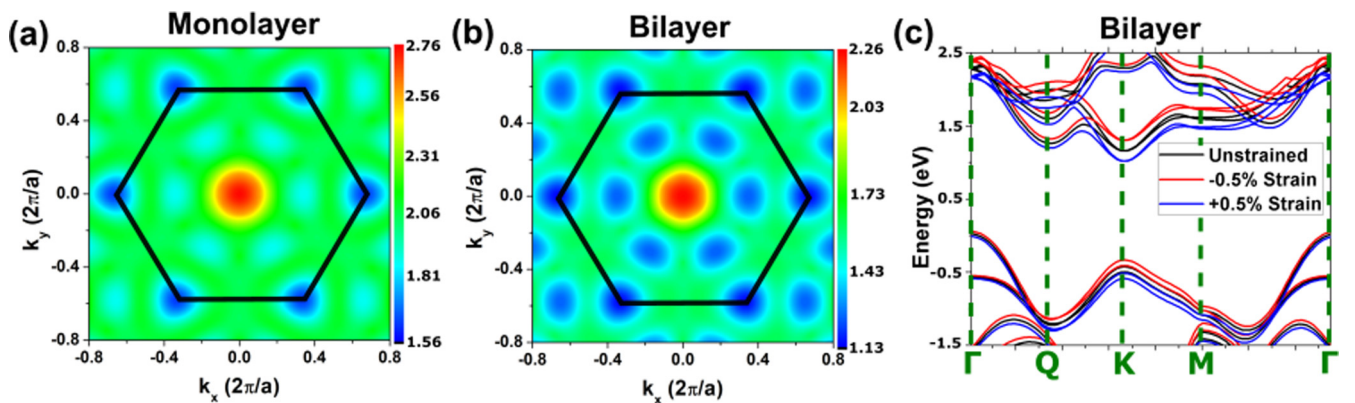


FIG. 3. Contour maps of the conduction band edge energy minimum calculated from density functional theory band structure simulations for (a) monolayer ( $a = 3.2139 \text{ \AA}$ ) and (b) bilayer ( $a = 3.2201 \text{ \AA}$ ) MoS<sub>2</sub>. We take  $E = 0$  to be at the corresponding top of the valence band in monolayer and bilayer MoS<sub>2</sub>. (c) Cut of the band structure along the high-symmetry directions in  $\mathbf{k}$  for unstrained (black curve),  $-0.5\%$  applied hydrostatic strain (red curve), and  $+0.5\%$  applied hydrostatic strain bilayer (blue curve) MoS<sub>2</sub>. The high-symmetry points ( $\Gamma$ ,  $Q$ ,  $K$ ,  $M$ ) are indicated by the green dashed lines.

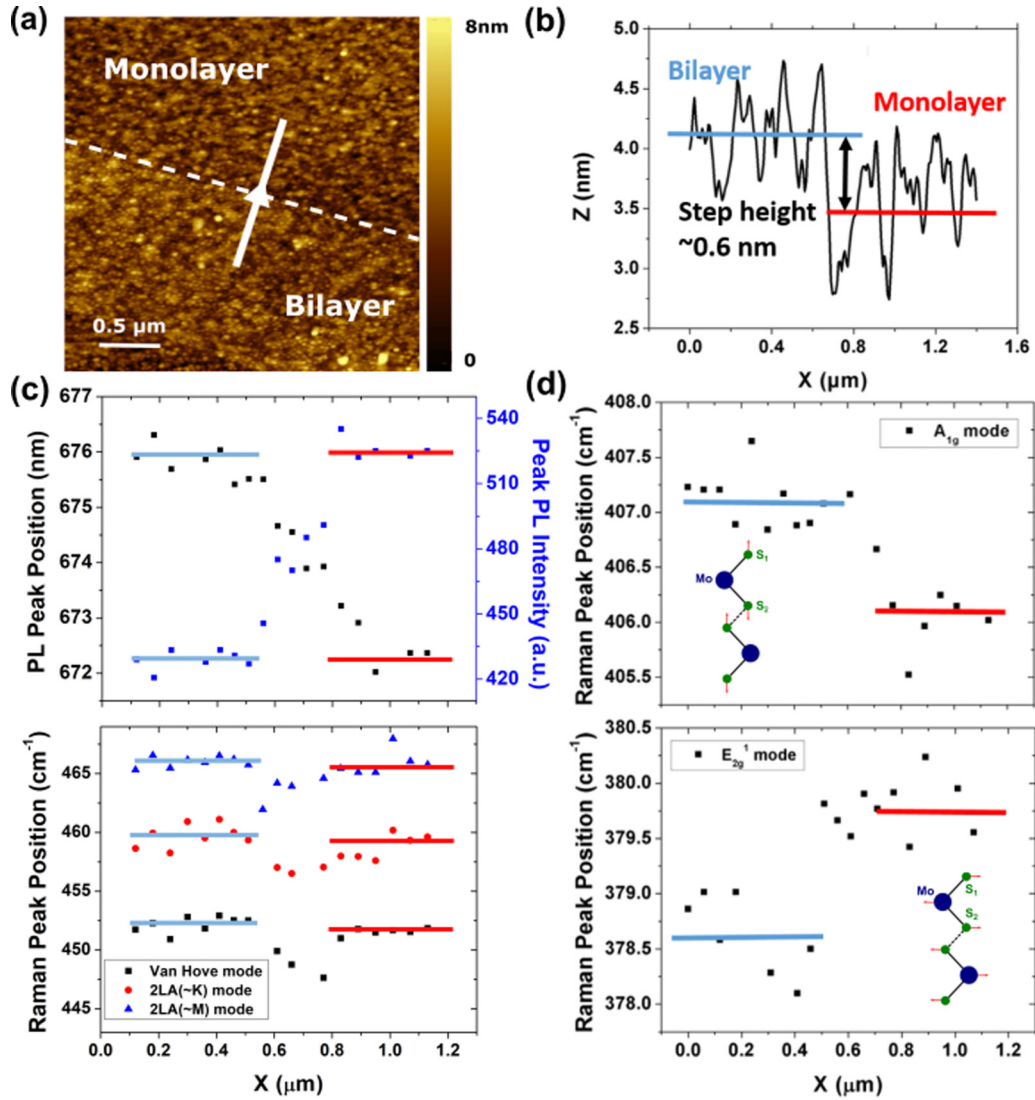


FIG. 4. (a) AFM image of MoS<sub>2</sub> transferred onto a flat Au substrate. The solid white line cut traverses a transition from a bilayer to a monolayer region, delineated by the white dashed line. (b) AFM topography for the white line cut shown in (a). The blue and red lines highlight the bilayer and monolayered regions, respectively, with a step height between the regions of ~0.6 nm. TEPL and TERS measurements taken along the line cut in (a) across the monolayer to bilayer transition region. The blue and red lines highlight the average constant values in the bilayer and monolayer regions. (c) Top panel: Position of the PL peak associated with the A exciton and trion (black points) and peak PL intensity (blue points) along the line cut. Bottom panel: Raman peak positions for the second-order Raman modes associated with the Van Hove singularity in the phonon DOS and scattering of electrons by longitudinal acoustic phonons near the K and M points in the BZ. (d) Raman peak positions for (top panel) first-order out-of-plane A<sub>1g</sub> mode and (bottom panel) second-order in-plane E<sub>2g</sub><sup>1</sup> mode. The insets for the top and bottom panels show schematic drawings for the movement of the atoms in the corresponding vibrational modes.

separate monolayer and bilayer regions in the MoS<sub>2</sub> that correspond very well with the topographic transition observed in AFM, with increasing layer thickness resulting, as expected, in a shift to longer wavelengths of the A excitonic peak position as well as decreasing peak PL intensity. As reported in previous work, there is significant PL quenching from the substrate specifically in monolayer MoS<sub>2</sub> that mitigates the change in PL intensity from monolayer to bilayer [34]. The width of the transition region from monolayer to bilayer, which includes TEPL spatial resolution and carrier diffusion lengths, is approximately half a micron. The transition region width of the TEPL measurement is comparable to carrier diffusion lengths reported on exfoliated few-layer MoS<sub>2</sub> [35], but it

should be noted that the MoS<sub>2</sub> we are measuring contains both monolayer and bilayer regions and is in close proximity to Au.

The top and bottom panels of Fig. 4(d) show the behavior of the first-order Raman peak positions associated with the out-of-plane A<sub>1g</sub> and the in-plane E<sub>2g</sub><sup>1</sup> vibrational modes, respectively, from the TERS measurements taken along the same line cut across the monolayer to bilayer transition region. The insets show corresponding schematics that illustrate the movement of the atoms for the corresponding vibrational modes. In previous work, increasing layer thickness of MoS<sub>2</sub> results in increasing separation between the Raman peaks associated with the E<sub>2g</sub><sup>1</sup> and A<sub>1g</sub> modes [22,36]. There is a clear delineation of the monolayer and bilayer regions with

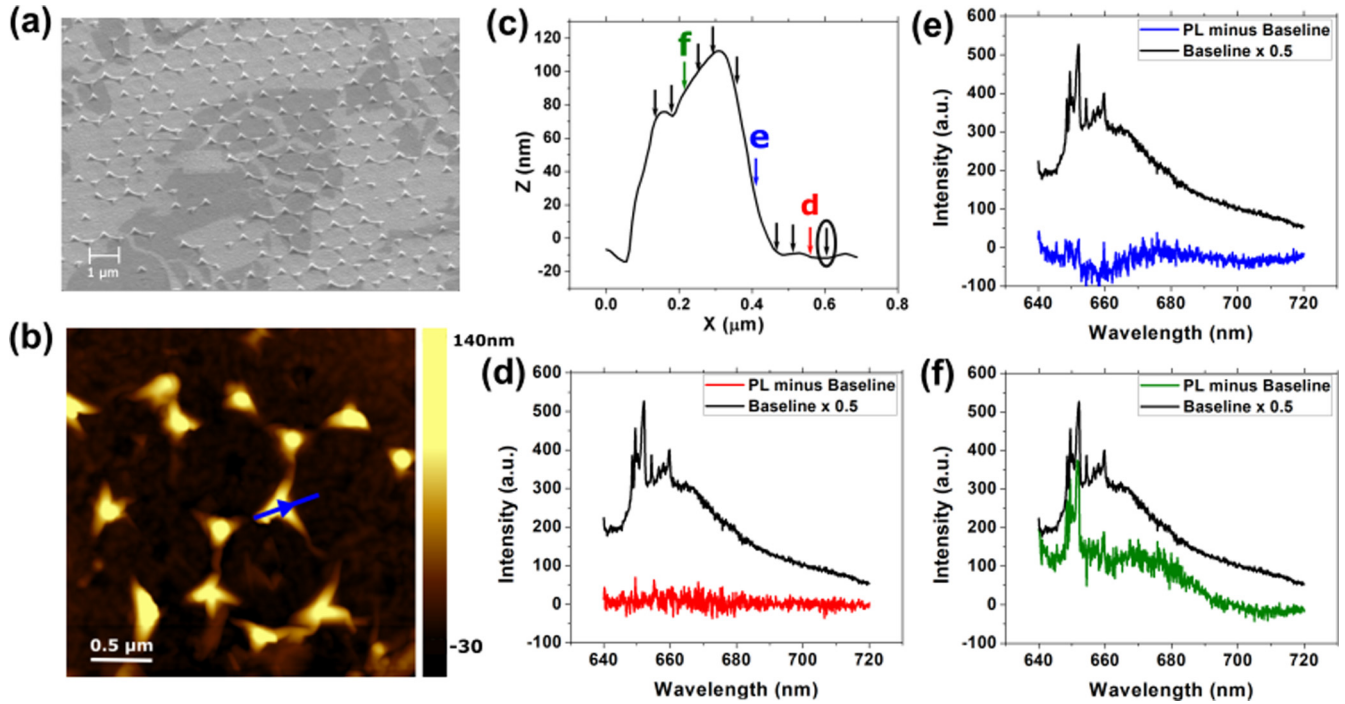


FIG. 5. (a) SEM image of successfully transferred MoS<sub>2</sub> on a patterned Au nanopyramid array. Areas covered by MoS<sub>2</sub> appear darker in the image. (b) An AFM image and line cut of bilayer MoS<sub>2</sub> draped over a Au nanopyramid. (c) AFM topography along the blue line cut in (b). Arrows indicate spatial position where TERS and TEPL measurements were taken. (d–f) TEPL spectra taken at points corresponding to the labeled arrows in (c). The black baseline PL spectrum is taken at the point indicated by the circled arrow.

the expected behavior of increasing layer thickness resulting in greater separation between the first-order Raman modes. The width of the transition region from monolayer to bilayer for the Raman peak position associated with the out-of-plane  $A_{1g}$  mode indicates a spatial resolution of approximately 100 nm, well below the illumination spot size of  $\sim 1 \mu\text{m}$  employed in these measurements. The separation observed between the  $E_{2g}^1$  and  $A_{1g}$  modes in the TERS experiments was  $\sim 26$  and  $\sim 29 \text{ cm}^{-1}$  for monolayer and bilayer MoS<sub>2</sub>, respectively, which is greater than the corresponding  $\sim 19$  and  $\sim 22 \text{ cm}^{-1}$  separation observed in conventional measurements with a 532-nm excitation laser performed on the same region of interest shown in Fig. 4(a). We believe the increased separation in the TERS measurements is due to a combination of factors. First, in the resonant Raman regime, the  $E_{2g}^1$  Raman peak has noticeable asymmetry with broadening occurring towards lower frequencies which would result in a shift of the peak position of the  $E_{2g}^1$  mode towards lower frequencies and a greater separation between the  $E_{2g}^1$  and  $A_{1g}$  modes. Second, the influence of the Au substrate can result in shifts in the peak positions for the  $E_{2g}^1$  and  $A_{1g}$  modes. Third, the unique electromagnetic enhancement of the TERS measurements could result in shifts in the peak positions in comparison to the conventional Raman case.

The bottom panel of Fig. 4(c) shows the behavior of the second-order Raman peak positions of modes associated with the Van Hove singularity in the phonon DOS and LA phonon scattering of excited electrons near the  $K$  and  $M$  points of the BZ from the TERS measurements taken along the line cut in Fig. 4(a). The peak positions are relatively

unchanged from monolayer to bilayer; however, there is a clear negative shift in the peak positions of all three modes near the interface between the monolayer and bilayer regions. The origin of these negative Raman shifts is currently being investigated.

## B. Strained MoS<sub>2</sub> on Au nanopyramids

By applying strain to MoS<sub>2</sub>, we can observe changes in the Raman and PL spectra that elucidate strain dependence in the band structure and phonon dispersion. We take advantage of the high spatial resolution of TERS demonstrated on a flat sample to probe strain inhomogeneity over submicron length scales. Using nanosphere lithography, we patterned an array of Au nanopyramids to induce strain on MoS<sub>2</sub>. Figure 5(a) shows a SEM micrograph of a patterned Au nanopyramid substrate with MoS<sub>2</sub> successfully transferred.

Figure 5(b) shows an AFM image and line cut of bilayer MoS<sub>2</sub> that has been successfully draped over a Au nanopyramid. The line cut goes from the end of one corner of the pyramid to the apex of the pyramid, where tensile strain would be highest, to finally a relaxed flat region. The topographic profile, shown in Fig. 5(c), yields a maximum height of  $\sim 120$  nm and width of  $\sim 400$  nm for the MoS<sub>2</sub> draped over the nanopyramid. To estimate the maximum strain induced on the MoS<sub>2</sub> at the apex of the pyramid, we employ two estimation methods—spherical pure bending [37] and buckle delamination [16]—which results in estimated maximum strains of 1.65% and 1.02%, respectively. (More details regarding strain calculations are found in the Supplemental Material [27], Sec. 3.)

We performed TEPL and TERS measurements at the points indicated by the arrows in Fig. 5(c). Figures 5(d)–5(f) show representative PL spectra taken at the points corresponding to the arrows with matching colors, with the red PL spectrum of Fig. 5(d) taken at a point on flat Au, the blue PL spectrum of Fig. 5(e) taken at a point on the slope of the nanopillar, and the green PL spectrum of Fig. 5(f) taken at a point near the apex of the nanopillar. The baseline PL spectrum, taken on a flat region, is taken at the point indicated by the circled arrow in Fig. 5(c). The entire evolution of the PL spectra along the line cut is shown in Sec. 5 of the Supplemental Material [27]. As shown in Fig. 3(c), tensile strain causes a decrease in both the  $\Gamma$ - $Q$  and  $\Gamma$ - $K$  band gaps in bilayer MoS<sub>2</sub>, which is analogous to the change in band gap in locally strained monolayer MoS<sub>2</sub> that induces an exciton funneling effect that also enhances and shifts the PL to longer wavelength [16]. The blue and green PL spectra in Figs. 5(e) and 5(f), respectively, reveal enhancement of the PL spectrum from  $\sim 670$  to  $\sim 690$  nm in wavelength, with additional luminescence shifted to longer wavelengths, which indicates a lowering of the band-gap energy in the locally strained bilayer MoS<sub>2</sub>. There is also a significant enhancement of the Raman modes in the green spectrum from  $\sim 645$  to  $\sim 660$  nm, which indicates that the unique geometry of the tip-sample junction at the apex of the nanopillar contributes to the TERS enhancement as well as the PL enhancement. The change in geometry especially affects the gap mode that forms between the tip and the Au substrate when the tip is within a few nanometers of the substrate. Further discussion about tip-sample geometry and signal enhancement can be found in the Supplemental Material [27], Sec. 5.

We have performed DFT simulations for monolayer and bilayer MoS<sub>2</sub> to estimate the effect of strain on the peak positions of the first-order Raman modes. With increased hydrostatic in-plane tensile strain there is a corresponding negative shift in the Raman peak position for both the  $E_{2g}^1$  and  $A_{1g}$  vibrational modes. The peak position of the in-plane  $E_{2g}^1$  Raman mode shows a greater negative shift due to the in-plane strain than the peak position of the  $A_{1g}$  out-of-plane mode. (Details about strain dependence DFT simulations are found in the Supplemental Material [27], Sec. 4.) The strain induced in MoS<sub>2</sub> by the Au nanopillar structures is not completely in-plane or hydrostatic, but the DFT simulations still provide a useful estimation for the strain dependence of the Raman modes.

Figure 6(a) shows the behavior of the Raman peak positions associated with the  $E_{2g}^1$  and  $A_{1g}$  vibrational modes, respectively, from TERS measurements taken along the same line cut of bilayer MoS<sub>2</sub> draped over the Au nanopillar with corresponding topography indicated in Fig. 6(c). Both the Raman peak positions of the  $E_{2g}^1$  and  $A_{1g}$  vibrational modes show a negative shift as the tensile strain increases at the apex of the nanopillar. The negative shift is larger for the in-plane  $E_{2g}^1$  mode when compared to the out-of-plane  $A_{1g}$  mode which agrees with both previous results [22] and DFT simulations. We do not observe significant splitting of the  $E_{2g}^1$  mode due to strain which has been observed to occur at uniaxial strains above 1.0%, which breaks symmetry [38]. The strain induced by the Au nanopillars is biaxial and does not contribute as significantly to symmetry breaking of the  $E_{2g}^1$  mode.

The effects of strain on the second-order Raman modes of MoS<sub>2</sub> have not been previously studied in detail. The

second-order Raman modes of MoS<sub>2</sub> related to DRR processes are sensitive specifically to changes in the momentum and energy conservation constraints that govern which transitions and states in the BZ participate in resonant interactions and in turn make them a useful tool to observe how strain causes distortions in the electronic band structure. Figure 6(b) illustrates the strain dependence of the second-order Raman modes from TERS measurements taken along the same line cut of bilayer MoS<sub>2</sub> draped over the Au nanopillar with corresponding topography indicated in the top panel. As shown in the second panel of Fig. 6(b), there is a negative shift of the Raman peak position of the second-order DRR mode associated with resonant scattering of excited electrons by both LA and TA phonons near the  $K$  point in the BZ (peak 3) as the TERS measurement location moves from the relaxed flat region to the region of highest tensile strain at the apex of the pyramid. Figure 6(c) shows the phonon dispersion for the acoustic phonon modes in bilayer MoS<sub>2</sub> calculated using DFT (the full phonon dispersion can be found in Sec. 4 of the Supplemental Material [27]). With positive applied hydrostatic strain, the calculated phonon dispersion indicates a negative shift in frequency for both the LA and TA vibrational modes at the  $K$  point, which would indicate a negative shift in the peak position both for peak 3 as well as for the peak position associated with only LA phonon scattering of excited electrons near the  $K$  point (peak 6). The third panel of Fig. 6(b) shows the behavior of Raman peak positions for peak 6, along the line cut of the nanopillar (the behavior of the remaining second-order modes is found in the Supplemental Material [27], Sec. 6). The position of peak 6 does not show significant strain dependence; however, experimental uncertainty in determining peak position may obscure strain dependence. From Fig. 2(a), peak 3 is isolated in frequency from the remaining second-order modes, which allows it to be fit more accurately and independently from the remaining second-order modes, such as peak 6.

We also observe a change in the peak areas of the second-order modes relative to each other. The bottom panel of Fig. 6(b) shows Raman peak areas of the second-order mode associated with LA phonon scattering of excited electrons near the  $K$  point in the BZ (peak 6) and the second-order mode associated with LA phonon scattering of excited electrons near the  $M$  point in the BZ (peak 7). From the figure and the corresponding topography, there is a clear increase in the area of peak 6 relative to that of peak 7 as tensile strain increases near the apex of the nanopillar. A decrease in the peak area of peak 6 relative to that of peak 7 has been previously observed in connection with the transition from monolayer to multilayer MoS<sub>2</sub>, where the  $K$  point and  $Q$  point conduction band minima become closer in energy as seen in Figs. 3(a) and 3(b) [24]. In the monolayer case, when the  $K$  point conduction band minimum is lower in energy than the  $Q$  point conduction band minimum,  $K$  to  $K'$  transitions mediated by the  $\mathbf{q}_{\sim K}$  acoustic phonons are much more prominent than  $K$  to  $Q$  transitions mediated by  $\mathbf{q}_{\sim M}$  phonons, as seen from the phonon density of states for allowed DRR processes in monolayer MoS<sub>2</sub>, as shown in Ref. [24]. In bilayer MoS<sub>2</sub>, because the difference in energy decreases between the  $K$  and  $Q$  points conduction band minima, many more transitions mediated by the  $\mathbf{q}_{\sim M}$  phonons will satisfy the constraints on a DRR process, which in turn increases the peak area of peak 7 relative to that of

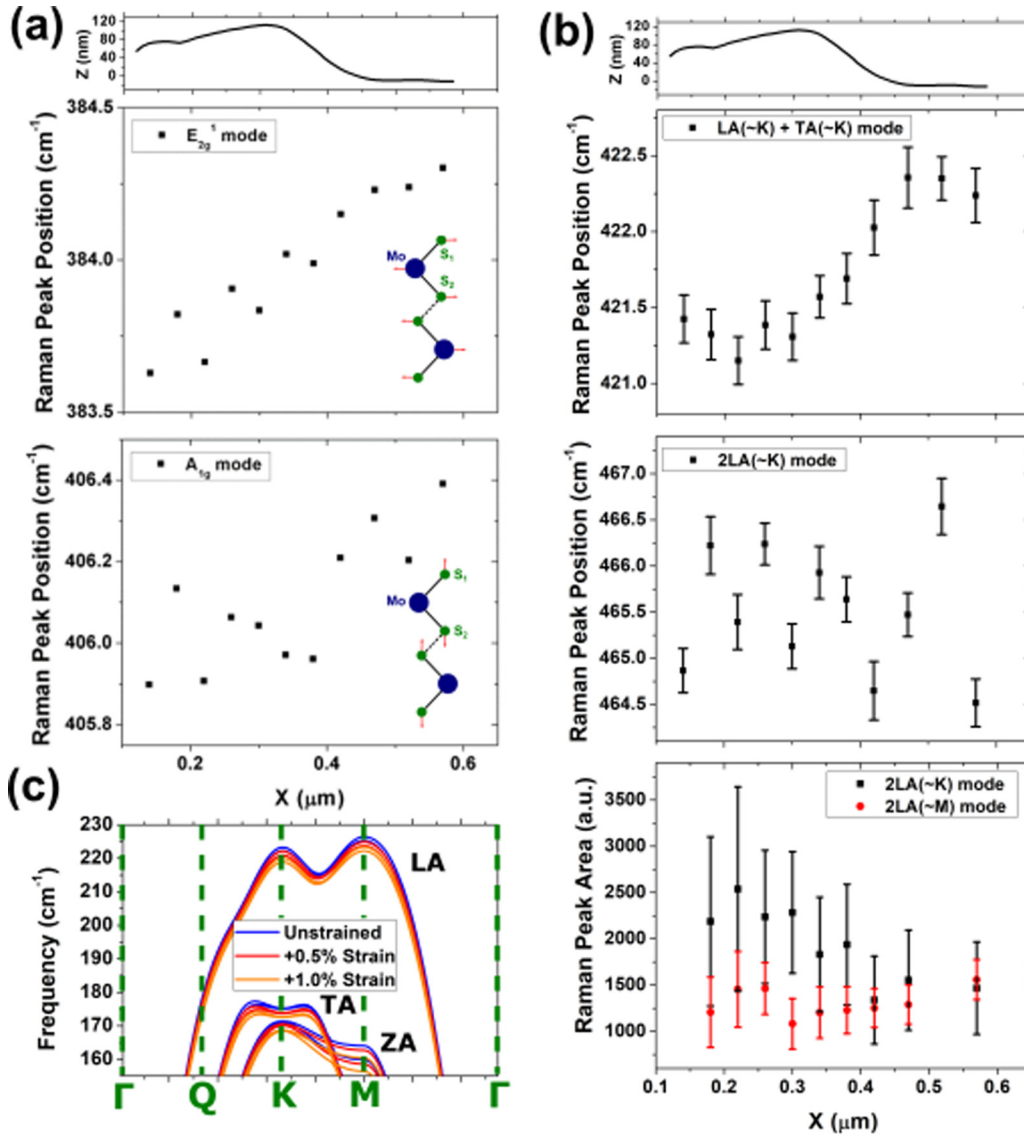


FIG. 6. (a) Top panel: AFM topography of the line cut shown previously in Fig. 5(b). Raman peak positions of the first-order (second panel)  $E_{2g}^1$  and (bottom panel)  $A_{1g}$  vibrational modes along the nanopillar line cut. The insets show schematic drawings of the movement of the atoms for the corresponding vibrational modes. (b) Raman peak positions (with error bars) of the second-order modes along the line cut (AFM topography shown in the top panel) related to (second panel) longitudinal and transverse acoustic phonon scattering of electrons near the  $K$  point in the BZ and (third panel) only longitudinal acoustic phonon scattering of electrons near the  $K$  point. Bottom panel: Raman peak areas (with error bars) of the second-order mode associated with LA phonon scattering of excited electrons near the  $K$  point in the BZ (black squares) and the second-order mode associated with LA phonon scattering of excited electrons near the  $M$  point in the BZ (red circles). (c) Phonon dispersion for the acoustic phonon modes calculated using DFT simulations for unstrained (blue curve), +0.5% applied hydrostatic strain (red curve), and +1.0% applied hydrostatic strain (orange curve) bilayer MoS<sub>2</sub>. The phonon modes represent the out-of-plane (ZA), in-plane transverse (TA), and in-plane longitudinal (LA) acoustic vibrational modes. The high-symmetry points ( $\Gamma$ ,  $Q$ ,  $K$ ,  $M$ ) are indicated by the green dashed lines.

peak 6. Figure 3(c) shows that with increased tensile strain, the conduction band minimum at the  $K$  point has a greater decrease in energy than the conduction band minimum at the  $Q$  point, which results in increased  $\mathbf{q}\sim\mathbf{K}$  phonon mediated transitions relative to  $\mathbf{q}\sim\mathbf{M}$  phonon mediated transitions. The increase in  $\mathbf{q}\sim\mathbf{K}$  phonon mediated transitions relative to  $\mathbf{q}\sim\mathbf{M}$  phonon mediated transitions is directly observed through an increase in the peak area of peak 6 relative to peak 7, which we see in the regions with greater tensile strain near the apex of the nanopillar.

#### IV. CONCLUSIONS

We have probed monolayer and bilayer MoS<sub>2</sub> using TERS and TEPL with clear subwavelength spatial resolution. Furthermore, we have created locally strained bilayer MoS<sub>2</sub> using patterned Au nanopillars and observed enhanced and shifted PL spectra in the areas of localized tensile strain, which we attribute to both a reduction in the band-gap energy as well as greater plasmonic enhancement from the gap mode. We have also probed the strain dependence of the second-order Raman spectrum in bilayer MoS<sub>2</sub>, revealing variations that



we attribute to changes in the electronic band structure and phonon dispersion due to tensile strain. By performing DFT simulations, we show that applying tensile strain affects the energy level of the conduction band minimum as well as the acoustic phonon dispersion, which confirms that changes in the second-order Raman spectrum functions as a useful probe for band structure and phonon mode behavior. Thus, resonant TERS characterization is shown to provide a powerful probe of strain, luminescence, electronic band structure, and phonon dispersion at the nanoscale. The information learned from these studies is likely to be important for a variety of TMDC-based devices including quantum emitters, and devices exploiting piezoelectric or flexoelectric effects at the nanoscale.

## V. COMPUTATIONAL DETAILS

We performed first-principles plane-wave calculations within density functional theory (DFT) executed in the PWSCF package of QUANTUM ESPRESSO [39] using ultrasoft pseudopotentials [40]. The exchange correlation potential was approximated by a generalized gradient approximation (GGA) using the PW91 functional [41]. Dispersion corrections using the DFT-D2 method were used during structural optimizations to determine the interlayer spacing in bilayer MoS<sub>2</sub> structures [42]. A vacuum spacing exceeding 10 Å was employed in the unit cells in order to separate adjacent supercells. A kinetic energy cutoff of 70 Ry was used, and the Brillouin zone was sampled using a Monkhorst-Pack grid [43] of  $25 \times 25 \times 1$  and  $15 \times 15 \times 3k$  points for monolayer and bilayer calculations, respectively. Atomic positions and lattice constants were optimized using damped molecular dynamics and the quick-

min Verlet algorithm. The Hellmann-Feynman force acting on each atom was limited to under  $3 \times 10^{-7}$  Ry per atomic unit, and the pressure in the unit cell was limited to less than 0.1 kbar. Structural optimizations yielded a lattice parameter of  $a = 3.2201$  Å, which is within 2% of the experimentally measured lattice parameter of 3.16 Å [44]. The calculated interlayer Mo-Mo spacing for bilayer MoS<sub>2</sub> is 6.2177 Å. Strain was applied to the lattice in the form of in-plane biaxial strain. In strained unit cells, atoms were relaxed along the axis perpendicular to the plane, but were otherwise fixed. Phonon vibrational frequencies were calculated using density functional perturbation theory (DFPT) as implemented in the PHONON package of QUANTUM ESPRESSO.

## ACKNOWLEDGMENTS

This work was partially supported by the Center for Dynamics and Control of Materials through the National Science Foundation MRSEC program under NSF Award No. DMR-1720595. Part of this work was supported by the NSF under Award No. DMR-1311866 and the Judson S. Swearingen Regents Chair in Engineering at the University of Texas at Austin. The growth of MoS<sub>2</sub> was supported by the Army STTR Award No. W911NF-14-P-0030. This work was performed in part at the University of Texas Microelectronics Research Center, a member of the National Nanotechnology Coordinated Infrastructure (NNCI), which is supported by the National Science Foundation (grant ECCS-1542159). The majority of the computational resources were provided by the Texas Advanced Computing Center at the University of Texas at Austin.

- 
- [1] E. Smith and G. Dent, *Modern Raman Spectroscopy—A Practical Approach* (John Wiley & Sons, Chichester, UK, 2005).
- [2] *Modern Techniques in Raman Spectroscopy*, edited by J. J. Laserna (John Wiley & Sons, Chichester, UK, 1996).
- [3] W. Bao, N. J. Borys, C. Ko, J. Suh, W. Fan, A. Thron, Y. Zhang, A. Buyanin, J. Zhang, S. Cabrini, P. D. Ashby, A. Weber-Bargioni, S. Tongay, S. Aloni, D. F. Ogletree, J. Wu, M. B. Salmeron, and P. J. Schuck, *Nat. Commun.* **6**, 7993 (2015).
- [4] A. M. Van Der Zande, P. Y. Huang, D. A. Chenet, T. C. Berkelbach, Y. You, G. H. Lee, T. F. Heinz, D. R. Reichman, D. A. Muller, and J. C. Hone, *Nat. Mater.* **12**, 554 (2013).
- [5] Y. Lee, S. Park, H. Kim, G. H. Han, Y. H. Lee, and J. Kim, *Nanoscale* **7**, 11909 (2015).
- [6] N. Hayazawa, Y. Inouye, Z. Sekkat, and S. Kawata, *Opt. Commun.* **183**, 333 (2000).
- [7] M. S. Anderson, *Appl. Phys. Lett.* **76**, 3130 (2000).
- [8] R. M. Stöckle, Y. D. Suh, V. Deckert, and R. Zenobi, *Chem. Phys. Lett.* **318**, 131 (2000).
- [9] Z. Zhang, D. C. Dillen, E. Tutuc, and E. T. Yu, *Nano Lett.* **15**, 4303 (2015).
- [10] K.-D. Park, O. Khatib, V. Kravtsov, G. Clark, X. Xu, and M. B. Raschke, *Nano Lett.* **16**, 2621 (2016).
- [11] S. Bertolazzi, J. Brivio, and A. Kis, *ACS Nano* **5**, 9703 (2011).
- [12] R. C. Cooper, C. Lee, C. A. Marianetti, X. Wei, J. Hone, and J. W. Kysar, *Phys. Rev. B* **87**, 035423 (2013).
- [13] Z. Yin, H. Li, H. Li, L. Jiang, Y. Shi, Y. Sun, G. Lu, Q. Zhang, X. Chen, and H. Zhang, *ACS Nano* **6**, 74 (2012).
- [14] Q. H. Wang, K. Kalantar-Zadeh, A. Kis, J. N. Coleman, and M. S. Strano, *Nat. Nanotechnol.* **7**, 699 (2012).
- [15] W. J. Yu, Z. Li, H. Zhou, Y. Chen, Y. Wang, Y. Huang, and X. Duan, *Nat. Mater.* **12**, 246 (2013).
- [16] A. Castellanos-Gomez, R. Roldán, E. Cappelluti, M. Buscema, F. Guinea, H. S. J. van der Zant, and G. A. Steele, *Nano Lett.* **13**, 5361 (2013).
- [17] C. Palacios-Berraquero, D. M. Kara, A. R.-P. Montblanch, M. Barbone, P. Latawiec, D. Yoon, A. K. Ott, M. Loncar, A. C. Ferrari, and M. Atatüre, *Nat. Commun.* **8**, 15093 (2017).
- [18] A. Branny, S. Kumar, R. Proux, and B. D. Gerardot, *Nat. Commun.* **8**, 15053 (2017).
- [19] S. K. Kim, R. Bhatia, T.-H. Kim, D. Seol, J. H. Kim, H. Kim, W. Seung, Y. Kim, Y. H. Lee, and S.-W. Kim, *Nano Energy* **22**, 483 (2016).
- [20] W. Wu, L. Wang, Y. Li, F. Zhang, L. Lin, S. Niu, D. Chenet, X. Zhang, Y. Hao, T. F. Heinz, J. Hone, and Z. L. Wang, *Nature* **514**, 470 (2014).
- [21] C. J. Brennan, R. Ghosh, K. Koul, S. K. Banerjee, N. Lu, and E. T. Yu, *Nano Lett.* **17**, 5464 (2017).

- [22] C. Rice, R. J. Young, R. Zan, U. Bangert, D. Wolverson, T. Georgiou, R. Jalil, and K. S. Novoselov, *Phys. Rev. B* **87**, 081307 (2013).
- [23] G. L. Frey, R. Tenne, M. J. Matthews, M. S. Dresselhaus, and G. Dresselhaus, *Phys. Rev. B* **60**, 2883 (1999).
- [24] B. R. Carvalho, Y. Wang, S. Mignuzzi, D. Roy, M. Terrones, C. Fantini, V. H. Crespi, L. M. Malard, and M. A. Pimenta, *Nat. Commun.* **8**, 14670 (2017).
- [25] Y. Liu, R. Ghosh, D. Wu, A. Ismach, R. Ruoff, and K. Lai, *Nano Lett.* **14**, 4682 (2014).
- [26] D. Lloyd, X. Liu, J. W. Christopher, L. Cantley, A. Wadehra, B. L. Kim, B. B. Goldberg, A. K. Swan, and J. S. Bunch, *Nano Lett.* **16**, 5836 (2016).
- [27] See Supplemental Material at <http://link.aps.org/supplemental/10.1103/PhysRevB.97.085305> for details on the transfer process, strain calculations, DFT simulations, and additional Raman data (N.D.).
- [28] Z. Yang, J. Aizpurua, and H. Xu, *J. Raman Spectrosc.* **40**, 1343 (2009).
- [29] H. Peelaers and C. G. Van de Walle, *Phys. Rev. B* **86**, 241401 (2012).
- [30] C. Lee, H. Yan, L. E. Brus, T. F. Heinz, J. Hone, and S. Ryu, *ACS Nano* **4**, 2695 (2010).
- [31] K. F. Mak, C. Lee, J. Hone, J. Shan, and T. F. Heinz, *Phys. Rev. Lett.* **105**, 136805 (2010).
- [32] A. Splendiani, L. Sun, Y. Zhang, T. Li, J. Kim, C. Y. Chim, G. Galli, and F. Wang, *Nano Lett.* **10**, 1271 (2010).
- [33] K. F. Mak, K. He, C. Lee, G. H. Lee, J. Hone, T. F. Heinz, and J. Shan, *Nat. Mater.* **12**, 207 (2013).
- [34] M. Buscema, G. A. Steele, H. S. J. van der Zant, and A. Castellanos-Gomez, *Nano Res.* **7**, 561 (2014).
- [35] R. Wang, B. A. Ruzicka, N. Kumar, M. Z. Bellus, H.-Y. Chiu, and H. Zhao, *Phys. Rev. B* **86**, 045406 (2012).
- [36] H. J. Conley, B. Wang, J. I. Ziegler, R. F. Haglund, S. T. Pantelides, and K. I. Bolotin, *Nano Lett.* **13**, 3626 (2013).
- [37] B. G. Shin, G. H. Han, S. J. Yun, H. M. Oh, J. J. Bae, Y. J. Song, C. Y. Park, and Y. H. Lee, *Adv. Mater.* **28**, 9378 (2016).
- [38] J.-U. Lee, S. Woo, J. Park, H. C. Park, Y.-W. Son, and H. Cheong, *Nat. Commun.* **8**, 1370 (2017).
- [39] P. Giannozzi, S. Baroni, N. Bonini, M. Calandra, R. Car, C. Cavazzoni, D. Ceresoli, G. L. Chiarotti, M. Cococcioni, I. Dabo, A. Dal Corso, S. De Gironcoli, S. Fabris, G. Fratesi, R. Gebauer, U. Gerstmann, C. Gougoussis, A. Kokalj, M. Lazzeri, L. Martin-Samos *et al.*, *J. Phys.: Condens. Matter* **21**, 395502 (2009).
- [40] D. Vanderbilt, *Phys. Rev. B* **41**, 7892 (1990).
- [41] J. P. Perdew, J. A. Chevary, S. H. Vosko, K. A. Jackson, M. R. Pederson, D. J. Singh, and C. Fiolhais, *Phys. Rev. B* **48**, 4978 (1993).
- [42] S. Grimme, *J. Comput. Chem.* **27**, 1787 (2006).
- [43] H. J. Monkhorst and J. D. Pack, *Phys. Rev. B* **13**, 5188 (1978).
- [44] T. Böker, R. Severin, A. Müller, C. Janowitz, R. Manzke, D. Voß, P. Krüger, A. Mazur, and J. Pollmann, *Phys. Rev. B* **64**, 235305 (2001).